Scene-based method for spatial misregistration detection in hyperspectral imagery

Dell'Endice, F ; Nieke, J ; Schläpfer, D ; Itten, K I

Abstract: Hyperspectral imaging (HSI) sensors suffer from spatial misregistration, an artifact that prevents the accurate acquisition of the spectra. Physical considerations let us assume that the influence of the spatial misregistration on the acquired data depends both on the wavelength and on the across-track position. A scene-based method, based on edge detection, is therefore proposed. Such a procedure measures the variation on the spatial location of an edge between its various monochromatic projections, giving an estimation for spatial misregistration, and also allowing identification of misalignments. The method has been applied to several hyperspectral sensors, either prism, or grating-based designs. The results confirm the dependence assumptions on and Θ, spectral wavelength and across-track pixel, respectively. Suggestions are also given to correct for spatial misregistration.

DOI: https://doi.org/10.1364/AO.46.002803

Scene-based method for spatial misregistration detection in hyperspectral imagery

Francesco Dell'Endice, Jens Nieke, Daniel Schläpfer, and Klaus I. Itten

Hyperspectral imaging (HSI) sensors suffer from spatial misregistration, an artifact that prevents the accurate acquisition of the spectra. Physical considerations let us assume that the influence of the spatial misregistration on the acquired data depends both on the wavelength and on the across-track position. A scene-based method, based on edge detection, is therefore proposed. Such a procedure measures the variation on the spatial location of an edge between its various monochromatic projections, giving an estimation for spatial misregistration, and also allowing identification of misalignments. The method has been applied to several hyperspectral sensors, either prism, or grating-based designs. The results confirm the dependence assumptions on λ and θ, spectral wavelength and across-track pixel, respectively. Suggestions are also given to correct for spatial misregistration.

OCIS codes: 080.1010, 100.6890, 120.6200, 300.6190.

1. Introduction

Spatial misregistration (SM) is an artifact that mainly affects pushbroom systems,[1] where contiguous ground pixels are recorded at the same time by an array-based detector, e.g., a CCD, in comparison to whiskbroom scanners,[1] which scan one ground pixel at a time, recording its spectral components. The study of this artifact is relevant to understand the quality degradation of the acquired data. The basic element in hyperspectral imaging (HSI) is the image cube[2] [Fig. 1(a)], which contains two spatial dimensions, and one spectral dimension. An x–y section of the cube is the monochromatic view of the sensed scene (also called the layer), while the y–z section represents one frame [Fig. 1(b)], which can be identified with either the sensor focal plane, or the image plane, i.e., the CCD. The pixels in one array line, i.e., the across-track dimension, correspond to the sampled ground spots. The spectrum of each ground spot is dispersed along one array column. In airborne and spaceborne applications the second spatial dimension (x axis), i.e., the along-track dimension, is provided by the motion of the platform, while in terrestrial sensors the two spatial dimensions are recorded temporally. Each pixel is then characterized by three indices (i, j, k). The hyperspectral image cube contains millions of picture elements (pixels), providing a rich source of information for identifying and classifying objects[3,4] with as much accuracy as possible. Nevertheless, there are a number of artifacts that degrade the image quality,[5] and result in nonuniformities in the acquired data. Uniformity can be intended as whatever makes the recorded data consistent with the actual data.

SM, one of these artifacts, is mainly investigated in this paper. The upwelling radiance, reflected by one ground pixel, should be decomposed in all its spectral components, along the same array column, at least in an ideal situation. SM alters this uniformity allowing the upwelling energy to decompose itself along more than one array column. It means that if two neighboring ground pixels contain two different target materials, with different spectra, then the spectrum measured by the sensor in one column will result in a mixture of the spectra of the two different materials. The objective of this work is to demonstrate that SM varies quadratically with wavelength and linearly with across-track position. First the physical causes for SM are analyzed, and later on a detection method is proposed.

2. Physical Reasons for Spatial Misregistration

SM is the sum of a high-order aberration and misalignments; the former refers to a distortion term in

The authors are with the Remote Sensing Laboratories (RSL), the Department of Geography, University of Zurich, CH-8057, Switzerland. F. Dell'Endice's e-mail address is fradel@geo.unizh.ch.

Received 6 October 2006; revised 5 December 2006; accepted 4 January 2007; posted 19 January 2007 (Doc. ID 75827); published 1 May 2007.

0003-6935/07/152803-14$15.00/0

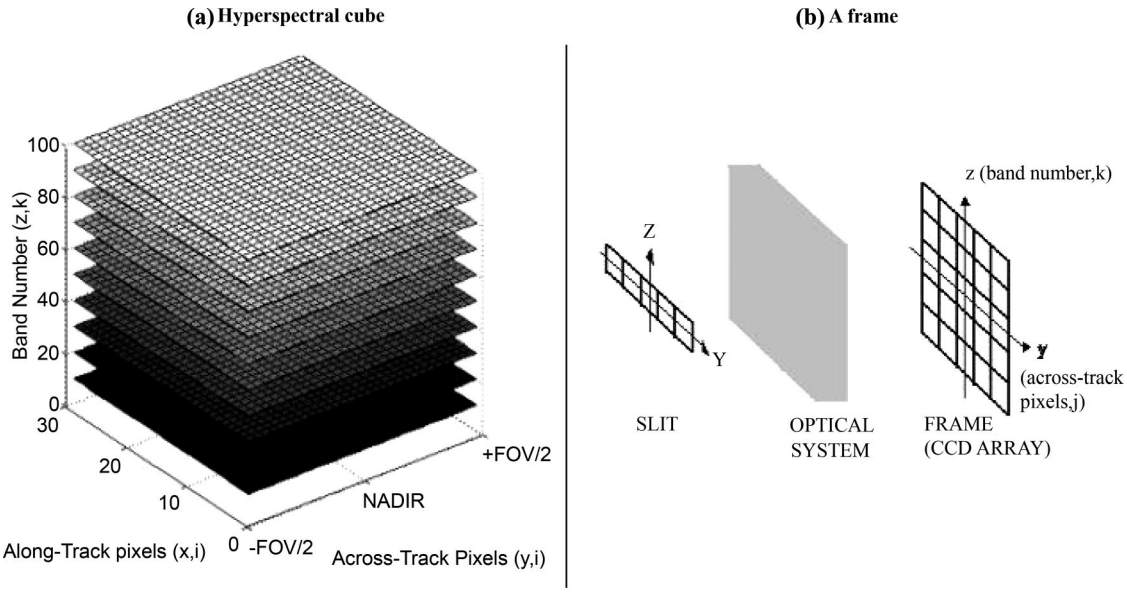

Fig. 1. (a) Various layers in a hyperspectral cube, (b) basic elements in a hyperspectral scanner. The *yz* plane is the main reference of this work.

the wave aberration function, while the latter refers to the arrangement of the sensor components. The distortion term is called keystone, which is sometimes erroneously used to address SM, as it gives the main contribution to this artifact. We want to point out that hereafter keystone is intended as an optical aberration only, and not as SM.

Keystone, as it is the case for the smile distortion,[6] acts in such a way that a straight line is not imaged in a straight line but rather in a curve.[6–8] The main contribution to keystone is given by the quadratic distortion II wave aberration (QAII).[9] An expression for this aberration, in the case of a prism is given in Eq. (1), while that for a plane grating is given in Eq. (2), as analyzed analytically in Ref. 8. (We used the formulas and notation of Ref. 8):

$$W_{\mathrm{QAII}} = -\frac{(1-n^2)}{n^2}\,\bar{u}\left[\bar{u}(\sin I_1 - \sin I_2')y - \frac{1}{2}(\sin I_1 + \sin I_2')\frac{ut}{n} - \Psi(\sin I_1 - \sin I_2')\right], \tag{1}$$

$$W_{\mathrm{QAII}} = -\bar{u}^2\left(\frac{m\lambda}{d}\right)y + \bar{u}\Psi\left(\frac{m\lambda}{d}\right). \tag{2}$$

This distortion is called quadratic because it depends quadratically on the field,[8,10,11] which we can identify with the focal plane. If we assume that the CCD pixel coordinate system (y, z) is centered on the focal plane [Fig. 1(b)], which applies to most of the available sensors, we can derive the following relationship:

$$\beta(y, z) = d(y, z)W_{\mathrm{QAII}}, \tag{3}$$

$$d(y, z) = y(c_1 z^2 + c_2), \tag{4}$$

where $\beta(y, z)$ is the keystone at position (y, z), $d(y, z)$ is the dependency coefficient in the same position, c_1 and c_2 are two proportionality constants, and y and z are the across-track, and the spectral dimensions, respectively. The expression for d suggests that keystone depends quadratically on wavelength [Fig. 2(a)] and linearly on the across-track pixel [Fig. 2(b)]. The quadratic dependence is symmetrical with respect to the y axis (i.e., changing of the parabola curvature sign), and increases when we move away from it. The whole keystone profile over the entire focal plane is shown in Fig. 2(c).

Misalignments between optical components influence the keystone profile, altering the position of the dispersed ray on the focal plane[12] and acting as an offset for it. The paraboloid [Fig. 2(c)] can be shifted either along the spectral axis, resulting in a vertical misalignment m_V [Fig. 3(a)], and/or rotate around the focal plane center, resulting in a rotational misalignment m_R [Fig. 3(b)].

We can now derive an expression for the SM, indicated with the variable s:

$$s(y, z) = \beta(y, z) + m_V + m_R, \tag{5}$$

where m_V, and m_R take in account for the offset, introduced by the two misalignments. Given a sensor, these two values are constant for all the focal plane elements. The SM can increase if two or more detector arrays are used to cover, for instance, a predefined spectral range: The overlapping regions generate the so-called coregistration.

We can also explain the spatial misregistration evaluating the detector response to the electromagnetic stimuli. Every pixel of the CCD is characterized by its spectral response function (SRF), and its point-spread function (PSF), the latter representing the sensor spatial response. If we assume that both the

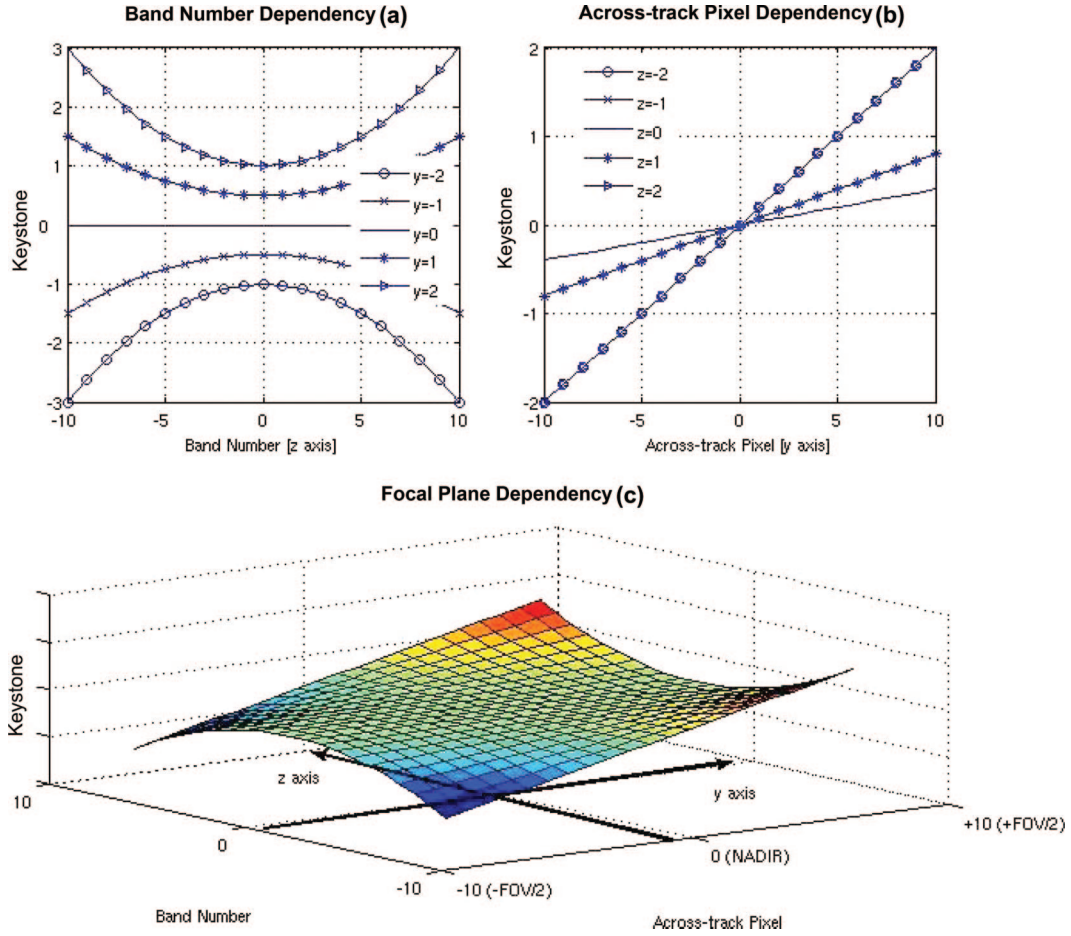

Fig. 2. (Color online) (a) Keystone variation with wavelength: Each curve corresponds to one spatial location. (b) Keystone variation with across-track position: Each curve corresponds to one band number. (c) The whole keystone variation over the focal plane.

SRF and the PSF are Gaussian-like functions, they can be distinctly identified by the FWHM and the peak location.[13] The combination of these two responses makes up the pixel response function (PRF), which, in an ideal system, has a 2D Gaussian shape (Fig. 4). Spatial uniformity[13] means that both the FWHM and the peak location of the PSF are constant over the spectrum (z direction), if they refer to the same across-track pixel. Generically, PSF nonuniformities correspond to variations of the FWHM and a peak location for each sort of response function, either spectral or spatial[14] (Fig. 4). In spite of that, hyperspectral imaging systems that have a SRF of nonuniform FWHM can efficiently gather information about a scene with a minimal corruption.[4]

3. State of the Art

SM affects the data in a manner that depends on the shape of the spectra to be recovered, and this makes it difficult to fix a requirement for such an artifact. Nevertheless, the maximum keystone has to be less than 5% of the pixel size.[6,14,15] This requirement is very stringent, but it is compulsory if we want spectral signatures useful for the science community. Strategies are then needed both to detect and to correct for it.

To avoid image distortions, new optical designs have been investigated, especially based on concentric optics,[6,16] to make both grating-based and prism-based sensors as accurate as possible. Concentric optics has been used for the Compact High Resolution Imaging Spectrometer (CHRIS)[17]; by introducing a field prism near the image plane, the image distortions can be corrected.[18] Moreover, if the optical system is plane symmetric (also called bilateral symmetric), the main dependence of aberrations as a function of system parameters has been established by a set of approximate aberration coefficients.[9] Conditions to make the optical system free from aberrations, which have quadratic dependence on the focal plane position, have also been studied.[11]

A pushbroom is usually preferred to a whiskbroom scanner because it offers a higher signal-to-noise ratio (SNR),[14,19] even if it experiences a few nonuniformities, which can be removed by means of careful calibration.[6] Nevertheless, whiskbroom sensors can present a constant SM, because of misalignments. Laboratory measurements are performed to quantify the SM. A pinhole, illuminated by a white source,[20] is imaged onto a CCD column (z axis), for a few spatial positions along the y axis. The gravity centers of the pinhole blurred images onto the pixel elements cor-

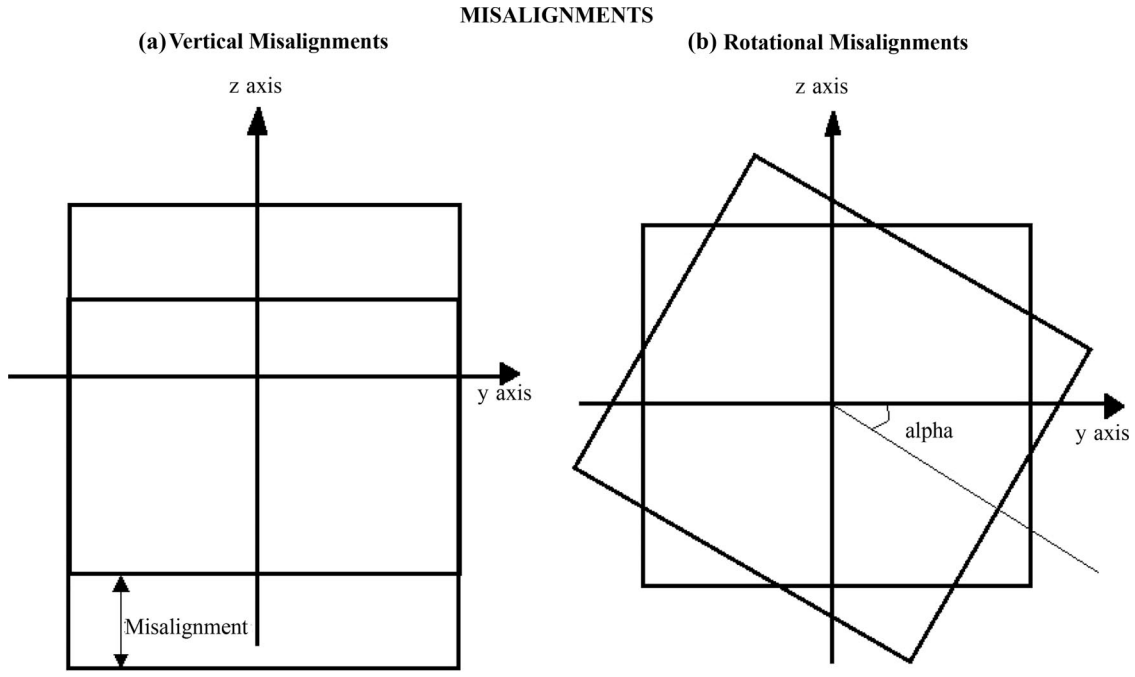

Fig. 3. (a) Vertical misalignment m_V, (b) rotational misalignment m_R.

respond to the PSF centers; their alignment gives a measure for SM. However, this procedure is time consuming; it implies that only a few locations along the field of view (FOV) can be measured. A complete analysis of the whole focal plane is not possible. Additionally, the laboratory calibration is usually performed once or twice per year. As each instrument may suffer from temporal instability (i.e., a changing of the calibration parameters with time), a few laboratory calibrations per year can be inadequate to characterize properly the instrument during its operational life (i.e., flight campaigns). On the other hand, several laboratory calibrations per year will continuously interrupt the flight sessions.

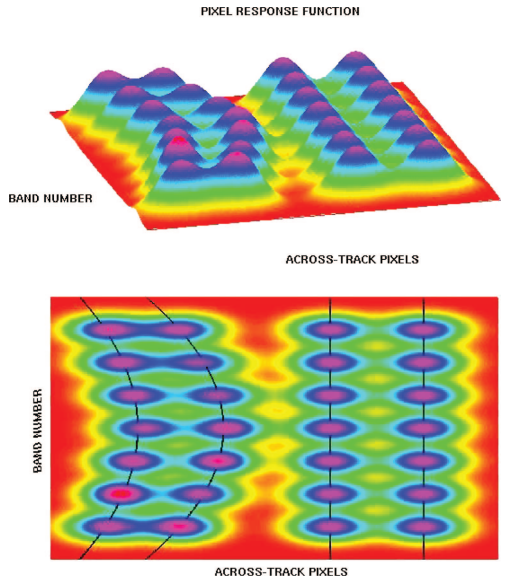

Fig. 4. (Color online) Two views of a CCD with 4 across-track pixels and 7 bands. The 2 across-track pixels at the right of the image do not have any SM because the peaks are all aligned. In the left-side pixels, there is some SM: In fact, the peaks are not aligned, but they are located on a curved line.

Data processing can be used then to improve the characterization of the sensor. Resampling, for instance, has been applied to the airborne hyperspectral imager (AHI), via a statistical approach, called "kriging,"[21] a correction procedure that transforms the actual radiance values to the desired ones. The desired values are computed on pixel basis using a weighting coefficient, which depends both on the expected error and on a set of calibration parameters. A detection method is also available and is based upon the edge detection.[22] It relies on the sensed scene, and it uses a Sobel filter to detect edges in each layer of the scene. One monochromatic view of an edge is chosen as a reference (e.g., zero SM), and a correlation analysis is then performed between this reference and the other monochromatic views of the same edge. This technique measures a series of subpixel shift values, which are an estimation for SM; such values are relative because they depend on the band chosen as reference. An invariant measure can be recovered by calculating a rms deviation of the shifts for each across-track pixel over all the spectral bands, but this will bring only one value for the whole frame. In the next section, we propose an improved version of this method, whose results are independent of the layer chosen as a reference.

4. Method

The following procedure analyzes the acquired scenes. Let us consider an image cube matrix **C**. We assume

that edges are present in the acquired scene, and for sake of easiness, we analyze only one of them, which extends for several along-track pixels, and for a few across-track pixels. If the sensor suffers from SM, both the orientation, and location of the edge will vary both with the wavelength and with the across-track pixel. The aim of the procedure is indeed to find the edge location, at subpixel level, in a given spectral band, and retrieve the same parameter for all the bands, and this will be estimation for SM. As the sampled image of an edge is blurred, by edge location we mean a point within this transition region whose exact position will be specified afterwards. In the notation, matrices are capitalized, while their elements are in lower case. The method can be summarized as follows:

1. *Selection*: If there is a noticeable edge, a subset of the image cube **C** is then selected manually, by means of visualization software. This can be accomplished observing a quick look of the scene. This produces a 3D matrix subset **B**, with p along-track pixels, q across-track pixels, and r spectral bands, and each **B** element will be indicated as $b(i, j, k)$.

2. *Desaturation*: Digital number values equal to the upper limit of the sensor dynamic range need to be changed to zero to avoid discontinuities during the edge sharpening. This step will generate the desaturated subset **D** with same dimensions as **B**:

$$\begin{aligned} &\text{If } b(i,\ j,\ k) = u, \text{ then } d(i,\ j,\ k) = 0 \\ &\text{else } d(i,\ j,\ k) = b(i,\ j,\ k), \end{aligned} \tag{6}$$

where u is the dynamic range upper limit.

3. *Sharpening*: The edge is sharpened using a first-derivative kernel, applied only in the across-track dimension (y direction), for the entire r layer. The gradient we used has the following expression:

$$\mathbf{G} = \begin{bmatrix} 1 & 1 & 1 & 0 & -1 & -1 & -1 \\ 1 & 2 & 2 & 0 & -2 & -2 & -1 \\ 1 & 2 & 3 & 0 & -3 & -2 & -1 \\ 1 & 2 & 3 & 0 & -3 & -2 & -1 \\ 1 & 2 & 3 & 0 & -3 & -2 & -1 \\ 1 & 2 & 2 & 0 & -3 & -2 & -1 \\ 1 & 1 & 1 & 0 & -1 & -1 & -1 \end{bmatrix}. \tag{7}$$

The filtered cube **T** will then be the convolution between the kernel gradient and the selected subset:

$$\mathbf{T} = \mathbf{G} * \mathbf{D}, \tag{8}$$

where $*$ denotes the convolution operation.

4. *Squaring*: The filtered cube is then squared in order to obtain positive maxima only:

$$\mathbf{F} = \mathbf{T}^2. \tag{9}$$

5. *Locating maxima*: For a given band $\bar{k}$ the pixel number corresponding to the derivative maximum in each ith line of the layer is found:

$$m(i)_{\bar{k}} = \max_j f(i,\ j,\ \bar{k}) \quad \forall i = 1,\ 2, \ldots,\ p. \tag{10}$$

$\mathbf{M}_{\bar{k}}$ is a column vector with p elements. The number of $\mathbf{M}_{\bar{k}}$ vectors will be equal to r. Locating an ideal edge is equivalent to finding the point where the derivative has a maximum (for a rising edge with positive slope) or a minimum (for a falling edge with negative slope). We can assume, without loss of generality, that the derivative has maxima only.

6. *Weighting*: For a give spectral band $\bar{k}$, a weighted sum around the maximum position is carried out for all the q lines:

$$\mathrm{v}(i)_{\bar{k}} = \frac{\left\lfloor \sum_{u=i-3}^{i+3} \sum_{j=m(i)-3}^{m(i)+3} \mathrm{c}(j) \cdot \left(\mathrm{f}(e,\ j,\ \bar{k})\right) \right\rfloor}{\left[\sum_{u=i-3}^{i+3} \sum_{j=m(i)-3}^{m(i)+3} \left(\mathrm{f}(e,\ j,\ \bar{k})\right)\right]}, \tag{11}$$

where $\mathrm{f}(e, j, \bar{k})$ is the derivative value for the pixel $u(i, j, \bar{k})$ in the kth band, and $\mathrm{c}(j)$ is a weighting factor for the pixel $u(i, j, \bar{k})$ whose value is linearly decreasing with the distance from the maximum position $m(i)$ along the across-track direction, being e a temporary index for i. The summation is taken over an odd number of columns and rows (usually 3, 5, or 7). The outcome of this operation will be r subpixel edge position vectors $\mathbf{V}_{\bar{k}}$, each one of them containing p elements.

7. *Averaging*: The mean across-track edge position, for each spectral band, is the averaging of the all p subpixel locations for that spectral channel:

$$\mathrm{z}(k) = \frac{\left\lfloor \sum_{i=1}^{p} \mathrm{v}(i)_k \right\rfloor}{p} \quad \forall \mathrm{k} = 1,\ 2, \ldots,\ r. \tag{12}$$

The next two steps are optional: They are useful for visualization (step 8), and analysis (step 9) purposes.

8. *Fitting*: The r elements of the **Z** vector are fitted using a second-order polynomial against the r bands.

9. *Comparison*: **Z** is compared with the available laboratory SM measurements.

It is apparent, that applying the method to several across-track pixels will provide the $s(y, z)$ profile.

There are different arguments that lead to the aforementioned procedure. In the literature there are several first-derivative kernels; some of them (i.e., Sobel,[23] Frei and Chan,[24] Prewitt[25]) are not suitable in the sense that they are not able to detect edges in a high-noise environment.[23] As the SNR is not uniform over the spectral range, this should be taken into account using an adequate detecting operator. A kernel, which performs well in such a case, is the Abdou[26] kernel that gives a linearly decreasing weighting to pixels away from the center of the edge. Obviously, one can use the kernel that better satisfies its requirements, but this has to be chosen attentively in accordance with the sensor characteristics. Second-derivative kernels have not been employed because they produce two-pixel-thick

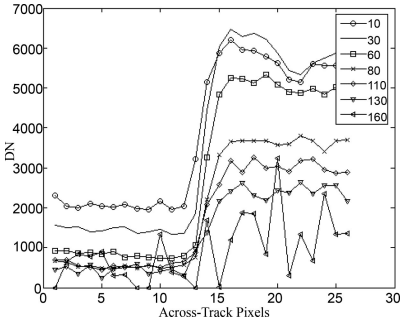

Fig. 5. An edge at different wavelengths, from the HYSPEX sensor. The edge is prominent from band 1 to band 110. In the last bands the derivative maximum disappears, and the edge is not detectable anymore.

edges, and they are extremely sensitive to noise. Besides, not all the spectral bands can be employed for the edge detection. The distinction between certain features can be clear, or at least evident in some region of the spectrum and blurred, or completely absent in other portions; this is because the spectral signature of the edge changes over the wavelength range (Fig. 5), and so the derivative maximum can be more significant in certain bands, and either less significant or completely absent in other bands. Edge detection is also influenced by the sensor performances, as is the SNR. The consequence is that in these bands the method fails. Bypassing this difficulty is achievable by selecting only the spectral channels with an acceptable contrast. Such a selection is done automatically by the method, in the sense that noisy bands will produce discontinuities in the **Z** vectors. Interpolation can be done afterwards to infer about the missing spectral information, but the interpolated value does not have any physical meaning unless we have some *a priori* knowledge.

The reason for a weighted sum is because in reality the maximum position is not corresponding to the exact edge location, but is rather an indication of where the edge center probably will be. This is for diffraction, aberrations, and optical issues that smooth the sampled image of the edge. Basically, we do not know *a priori* which band gives the absolute edge position to be used as a standard reference for all the spectral bands; it implies that there is an offset somewhere. If we assume that SM has a quadratic dependence on wavelength, then there will be a point (i.e., a band) where SM is the lowest. Ideally, this point will coincide with the band number located on the y axis [Fig. 1(b)]. We assume that the values measured in this spectral band will be the offset that we have been looking for, i.e., the minimal spatial misregistration values. In a real application, this reference point will be along an axis parallel to the y axis because of misalignments for instance.

5. Results and Discussion

The detection method has been applied to several pushbroom sensors, where AVIRIS[27] is the only whiskbroom scanner considered (Table 1). For each sensor, by means of various image cubes, several across-track positions have been analyzed, but in the next figure only three spatial positions are shown: $-$FOV/2, NADIR, and $+$FOV/2, which correspond to across-track pixels close respectively to $j_1 = 1$, $j_2 = q/2$, and $j_3 = q$, where q is the number of across-track pixels. The y axis, and the z axis are oriented as in Fig. 1(a). To improve the results, the data corresponding to neighboring across-track pixels have been averaged together, and standard deviation is the discriminant criteria in removing misregistration values out of the interval of confidence. The vertical axis corresponds to the spectral range while the horizontal axis corresponds to SM in a fraction of a pixel size [Fig. 1(b)].

Our objective will be to show that SM depends quadratically on wavelength and linearly on across-track position: Namely, we expect no SM along the j_2 column, and SM, equal in absolute value but opposite in sign, along j_1 (i.e., $-$FOV/2), and j_3 (i.e., $+$FOV/2).

As other artifacts and detector misalignments prevent this ideal behavior, we expect the SM variation to be slightly different and, in other words, the minimal linear variation to be along the NADIR direction, and a symmetrical variation on the rest of the focal plane. For a few sensors, SM laboratory measurements were available, and they will be used to validate the method.

A. HYSPEX

HYSPEX is a series of compact, high-resolution imaging spectrometers that is being developed by Norsk Elektro Optik AS, (NEO, Norway).[28] The instrument is modular and consists of three different spec-

Table 1. List of the Analyzed Sensors

Sensor	Scanner	Bands	Spectral Range [nm]	FOV [°]	Across Track Pixels	Dispersing Element	Image Acquisition Date
HYSPEX	Pushbroom	160	400–2500	17	1600	Grating	2005
PHILLS	Pushbroom	128	386–1003	30	1024	Grating	2004
AISA Eagle	Pushbroom	126	400–990	36.7	941	Prism-Grating-Prism	2005
HYPERION	Pushbroom	220	357–2576	0.63	256	Grating	2004
CHRIS	Pushbroom	37	440–1020	0.66	383	Prism	2005
CASI 3	Pushbroom	288	380–1050	39	1490	Prism	2006
AVIRIS	Whiskbroom	224	400–2500	34	677	Grating	2003

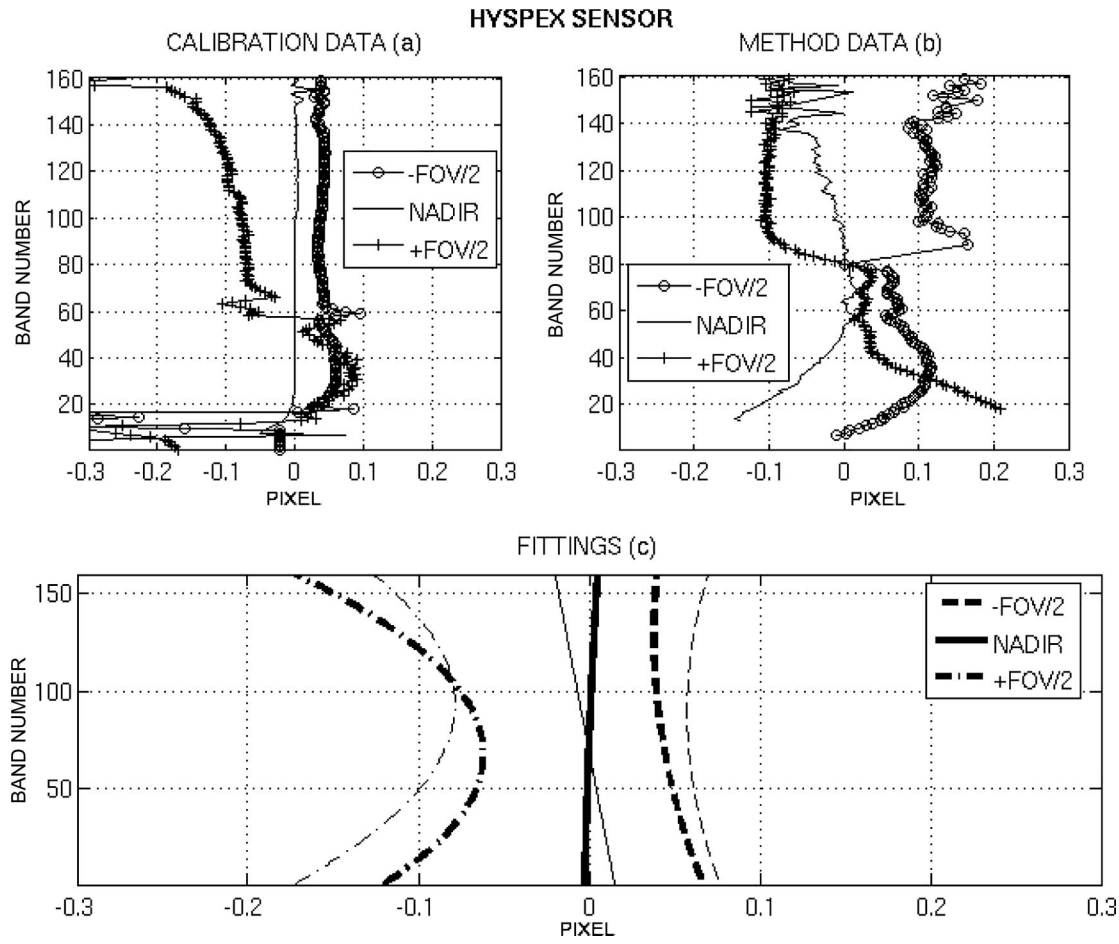

Fig. 6. (a) HYSPEX laboratory measurements: the three curves, starting from the left side, represent the spatial misregistration at +FOV/2, NADIR, and −FOV/2, respectively. (b) HYSPEX method analysis: plotting of the spatial misregistration data retrieved using the proposed procedure. (c) HYSPEX fittings: the thicker fittings represent laboratory data. The +FOV/2 curves have been plotted not considering the step attributable to the filter mask. The method overestimates the spatial misregistration.

trometer modules. We considered a prototype of the VNIR-1600 module. The latest release of the VNIR instrument has similar general specifications but improved optical quality.

The HYSPEX team provided a set of laboratory SM measurements [Fig. 6(a)], acquired using a broadband point source, which was located at three positions along the FOV at 1 m object distance. A simple singlet lens was inserted in the entrance aperture to achieve a good focus at this distance. It is important to notice that this lens slightly changes the optical image quality, which can explain discrepancies between the laboratory and airborne results. Furthermore, it should also be noted that the point source used was not perfect, as it had a size of approximately $\frac{1}{3}$ of a pixel, and the lamp available at the time of the measurements had a very low response in the blue range. For the laboratory measurements, SM is almost zero along the nadir direction; it becomes positive at −FOV/2 and negative at +FOV/2. Quantitatively, SM ranges from −6.63% to +2.24%. In the two sets of data, corresponding to the borders of the FOV, there is a step around band number 60, which is more prominent at +FOV/2. The step could arise because the PSF is of the order of only 1 pixel. For band numbers below 60, most of the energy is contained within one pixel column, and a signal level close to 0 is measured in the adjacent spatial pixel row. Above band 60, because of the small amount of the SM effect, the signal level in the adjacent pixel row gets large enough to shift the center of gravity of the energy distribution. The sudden shift can thus be viewed as a kind of quantization noise, and the position of this sudden shift can be altered by moving the point source in the along-track direction. The second-order filter mask could partly cause this shift, as the shift is located around the spectral bands at the border of the filtered region. The next figure [Fig. 6(b)] shows the data we obtained using the proposed scene-based method. The data out of the interval of confidence have been removed after filtering. In general, the variations are close to those described in the laboratory set: There is almost no SM along the nadir, and positive and negative SM at −FOV/2, and +FOV/2, respectively. In this case, a step is also present but it occurs at approximately band number 80 instead of being at approximately band number 60. The measurements related to the first 16 bands

are missing because the SNR in this part of the spectral range is low. The method, as expected, gives higher values owing to the not standard conditions experienced during the flight; in fact, SM, on average, ranges from −10.39% to 6.29%. There is an overestimation at approximately 4%, in absolute value, of the pixel size. We fit both the laboratory data, and the results of the proposed method with a quadratic polynomial [Fig. 6(c)]. In this plot, the thicker curves correspond to laboratory data while the thinner curves correspond to the results. Even if the fitting curves at both −FOV/2 and +FOV/2 exhibit a quadratic shape, we cannot infer about the SM quadratic dependence on wavelength, because of the mentioned step, but we can see at least a linear dependence on the across-track pixel between band number 90 and band number 160. The NADIR fitting is tilted around the focal plane center, and it implies a rotational misalignment. It should be noted that the VNIR-1600 has a physical pixel size of only 7.4 μm, corresponding to a FOV of 0.187 mrad, so the misalignment is very small; the vertical misalignment is almost absent, being the fitting lines symmetrical around the y axis. As the minimal SM is around band number 80, we can therefore assume this channel as the offset to be removed from the SM values corresponding to the other spectral channels. To measure quantitatively the similarity between these curves, we compare, in each of the three FOV positions, the excursion range, which is defined in absolute value, as the difference between the maximum and the minimum value for each fitting. The difference is approximately 0.01 pixels at −FOV/2, approximately 0.03 pixels at NADIR, and approximately 0.02 pixels at +FOV/2; it implies that the agreement is high, if we also consider that we are working at a very subpixel level.

B. PHILLS

The Ocean Portable Hyperspectral Imager for Low-Light Spectroscopy (Ocean PHILLS)[29] is used mainly for imaging the coastal ocean. We analyzed two versions of this instrument: The first has a focal length

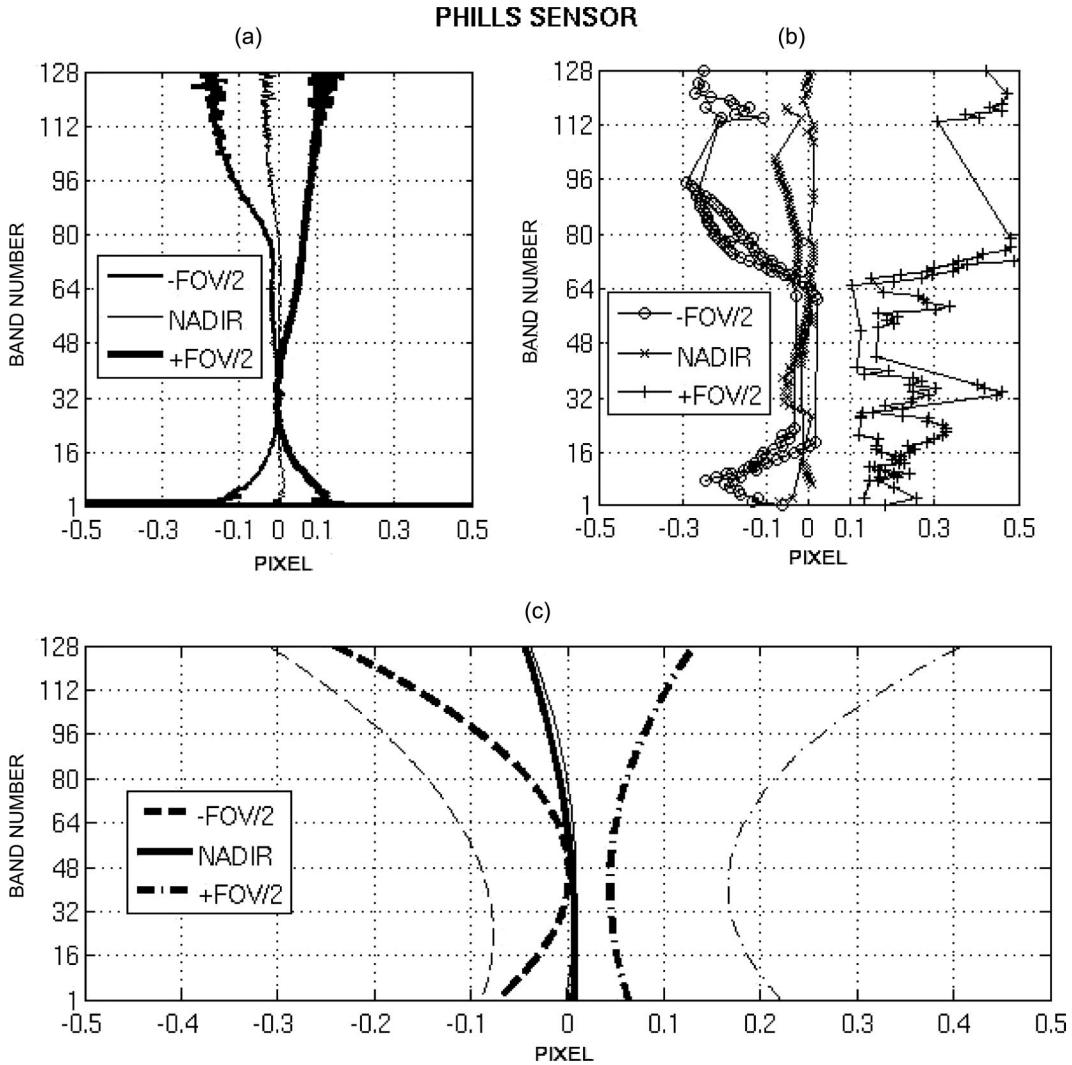

Fig. 7. (a) The sets of laboratory measurements: The blocking filter influence is evident after band number 64. (b) The data retrieved from the method: spatial misregistration at +FOV/2 is higher that that at −FOV/2. (c) Comparison between fittings.

of 12 mm, and the second has a focal length of 17 mm. PHILLS could provide up to 512 spectral channels, but our data have been binned by 4, and this leads to 128 bands.

A set of laboratory SM measurements was available [Figure 7(a)]; they were taken placing the sensor at the output of a collimator, a large off-axis parabola, which projects a geometric image of approximately 0.1 pixel. The aperture image on the CCD plane is wavelength dependent, and this gives a measure of SM. The data show how SM is almost absent along the NADIR direction, positive at +FOV/2, and negative at −FOV/2. SM is, in absolute value, under 10% of a pixel size, except beyond band number 96. Basically, SM becomes more evident after band number 64. The reason for this is because a blocking filter has been used: in fact, second-order diffractions, coming from the lower spectral range (between 380 and 500 nm) are falling between 760 and 1000 nm; a filter has been mounted behind the spectrometer, and it blocks wavelengths below 530 nm. In reality, the filter adds an offset in the bands where it is present. It should also be noticed that SM toward +FOV/2 is higher than that around the −FOV/2 pixels, and this could be attributable to some straylight. The SM values, retrieved applying our method to the PHILLS acquired scene [Fig. 7(b)], are slightly higher than those obtained in the laboratory. As from laboratory investigations, the SM increases after band number 60. The SM is negative at −FOV/2, below 2% around the NADIR direction, and positive at +FOV/2. We also notice here that SM is higher at +FOV/2. The fitting lines [Fig. 7(c)] make clear how the method overestimates SM; the bold curves represent the laboratory data. Even if after band number 64, the SM values seem to change in a quadratic way, we cannot prove a quadratic dependency on wavelength; we can claim a linear dependence on across-track pixels between band number 50 and band number 128. There is no symmetry around the y axis, and this lets us assume a vertical misalignment. Anyway, this sensor has an optical design where the lenses and the spectrometer do not share the same optical axis. In fact, the NADIR direction is at approximately pixel 460 nm, and it means that the optical axis does not intersect the focal plane in its center (i.e., along band number 64). This can be clearly identified from the fitting curves, which have a change in their first-derivative slope not around band number 64, but between band number 16 and band number 48. It implies that the layer at 460 nm can be used as the SM offset for the other spectral channels. Considering the fitting curves related to the method, we note a SM, on average, going from −14.05% up to 22.69%.

C. AISA Eagle

The Airborne Imaging Spectrometer (AISA)[30] uses a prism-grating-prism (PGP) as a dispersing element. There were no laboratory measurements available for this sensor. The data out of the interval of confidence, which we set equal to two mean deviations, have been removed. The SNR was good enough to let us apply the method almost over all the spectral range.

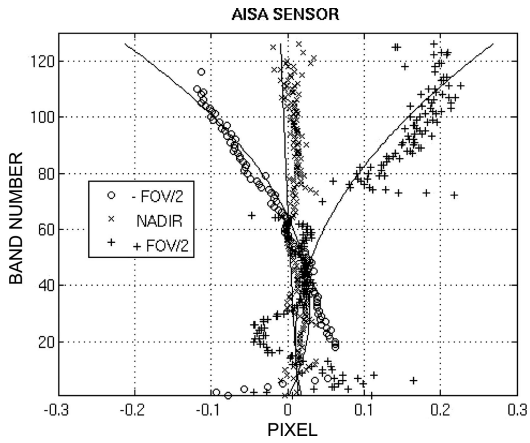

Fig. 8. AISA analysis. The plot shows a quadratic dependence of keystone on the focal plane and symmetry around the nadir axis. The focal plane has no rotational misalignment, but a slightly negative vertical misalignment.

The SM (Fig. 8) is almost zero in the middle of the focal plane; then it becomes negative when we move toward the −FOV/2, and it ranges from −1% to −11.5%. The SM is positive on the right side of the CCD, but it goes up to 19%.

Both the data and fitting lines show this time a quadratic variation with wavelength and a linear variation with across-track pixels. The symmetry around the z axis is apparent, meaning that there is no rotational misalignment. The fitting first-derivative sign is changing at approximately band number 30; there is no symmetry around the z axis, which supposes to pass by band 63, implying that there is little vertical misalignment. The optical axis does not pass by the CCD center, but it intersects the focal plane slightly below it. This behavior also suggests that the offset band should be taken from the first bands of the spectral range.

D. HYPERION

Hyperion,[31] in orbit since 2000, consists of a visible near-infrared detector (VNIR), and a shortwave infrared detector (SWIR). The instrument has a spatial resolution of 30 m for all bands. Laboratory data were not available.

The SWIR detector [Fig. 9(a)] has no SM along the NADIR direction; the artifact is positive at −FOV/2, and negative at +FOV/2, respectively. On average, the SM varies between 5.11% (at −FOV/2) and −2.32% (at +FOV/2). The SWIR fitting lines [Figure 8(a)] show that this detector has no rotational misalignment; in fact the NADIR SM line is parallel to the z axis. The symmetry that these lines have around the axis passing by band number 150 implies that the focal plane center is almost on the optical axis itself, which means no vertical misalignment. Band number 150 then exhibits the lowest SM. In this case, the quadratic variation with wavelength is

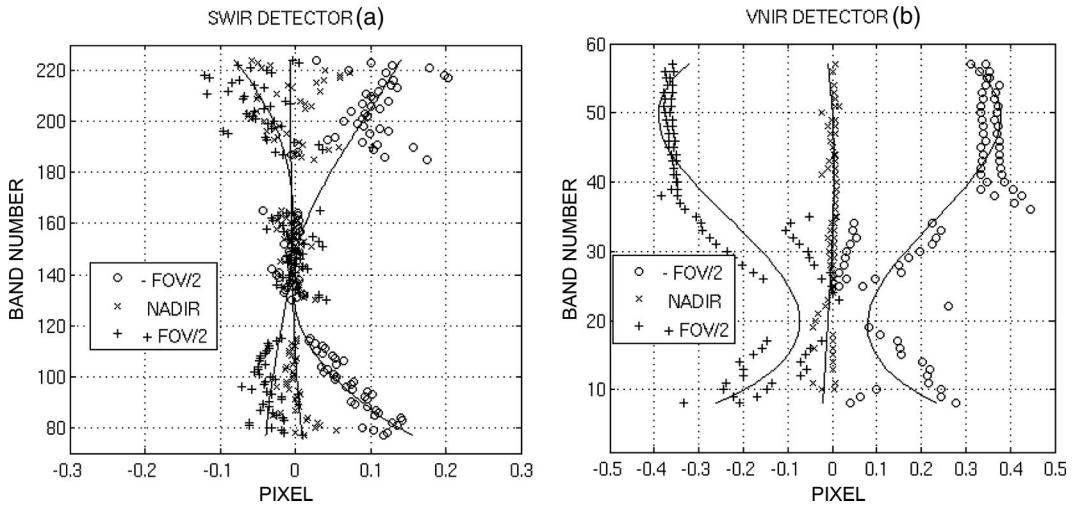

Fig. 9. (a) HYPERION SWIR analysis: SM is positive toward −FOV/2, and negative toward +FOV/2. The SWIR detector is well aligned, and also centered. Some bands are missing because of a low SNR. (b) HYPERION VNIR analysis: Spatial misregistration is higher than in the HYPERION SWIR detector. This detector has no rotational misalignment.

apparent even if few bands are missing because they were too noisy.

The VNIR detector shows a different situation [Figure 9(b)]. In general, the SM is negative at +FOV/2, approaching zero around the NADIR direction, and positive at −FOV/2. In this case, the method produces higher values than those obtained for the SWIR detector: on average, the SM goes from −22.96% up to 22.61%. We also notice that in the last 20 bands, SM is almost constant, and approximately 38.2% in absolute value; the main SM excursion (from 10% to 40% in absolute value) occurs before band number 40, and this is probably attributable to the SNR of the VNIR detector, which is low on the first spectral wavelengths. We decided to break down the spectral range to use two different fittings, the first going from band number 0 to band number 40, and the second for the other bands. The NADIR fitting line is parallel to the z axis, and once again it implies that the NADIR axis is perpendicular to the optical axis. There is no symmetry around the y axis; because of the reasons explained before, we suggest using band number 40 as the offset for all the other VNIR spectral channels.

E. CHRIS

CHRIS[18] is a spaceborne scanner, which has been in orbit since 2001. It can be used with different acquisition modes, and our data have been collected in MODE V. As we mentioned before, CHRIS uses curved prisms, but the surfaces are all spherical, and only one material is used for all the prisms. There are no laboratory data available, but the method results are worth discussing because the prism used is curved.

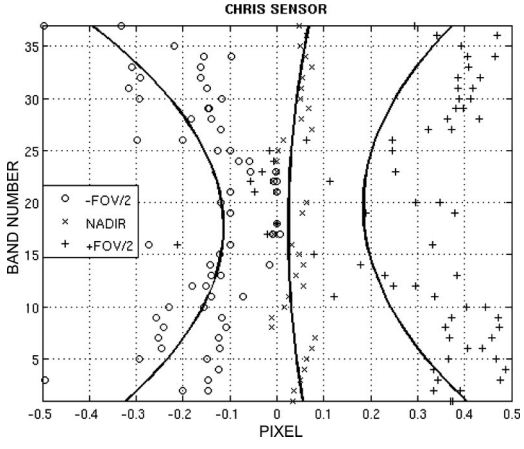

Fig. 10. CHRIS analysis: Nadir line does not coincide with the nadir direction, but it is slightly shifted aside; we may suppose that the instrument is slightly misaligned with the other optical components.

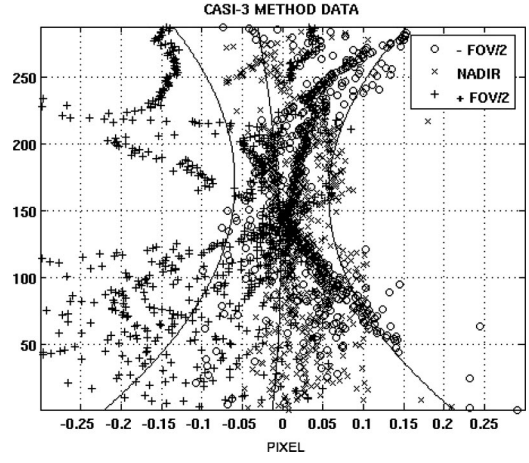

Fig. 11. CASI-3 analysis: Spatial misregistration profile shows a symmetry, which implies that the sensor is well aligned to the other optical parts, with no misalignments.

The SM profile (Fig. 10) shows the following behavior: The SM is constant along the NADIR direction, positive for pixels located at +FOV/2, and negative for pixels located at −FOV/2. The SM is slightly higher on the right side of the focal place: The mean value in this side is approximately 26% of a pixel, while on the opposite side it is approximately 20%. The average SM along the nadir is approximately 4% of a pixel size. The fitting lines have symmetry at approximately both the z axis, and the y axis, passing by band number 18; this implies that the focal plane has neither vertical misalignment nor rotational misalignment. The focal plane center lies on the optical axis. This also means that the values corresponding to the 18th band can be used as an offset for all the other channels. Nevertheless, the NADIR fitting curve does not coincide, within a really low percentage, with the NADIR line, and it may be because the CCD center is a little bit aside from the optical axis.

F. CASI-3

The Compact Airborne Spectrographic Imager[32] (CASI) is a VNIR sensor manufactured by ITRES Research Ltd., Canada. The SNR profile allows all the spectral range to be explored, and only a few results have been removed from the interval of confidence. The analysis has been conducted over several subsets, extracted from the available hyperspectral cubes.

The SM profile (Fig. 11) exhibits a quadratic dependence on the CCD array positions. The SM is constant, and close to zero, along the z axis; it becomes positive if we move toward pixels at approximately −FOV/2, while it is negative in the opposite direction. On average, the SM varies between 10.04% (at −FOV/2) and −10.15% (at +FOV/2), being 0.98% along the NADIR direction. The SM is higher at both limits of the spectral range, and this is attrib-

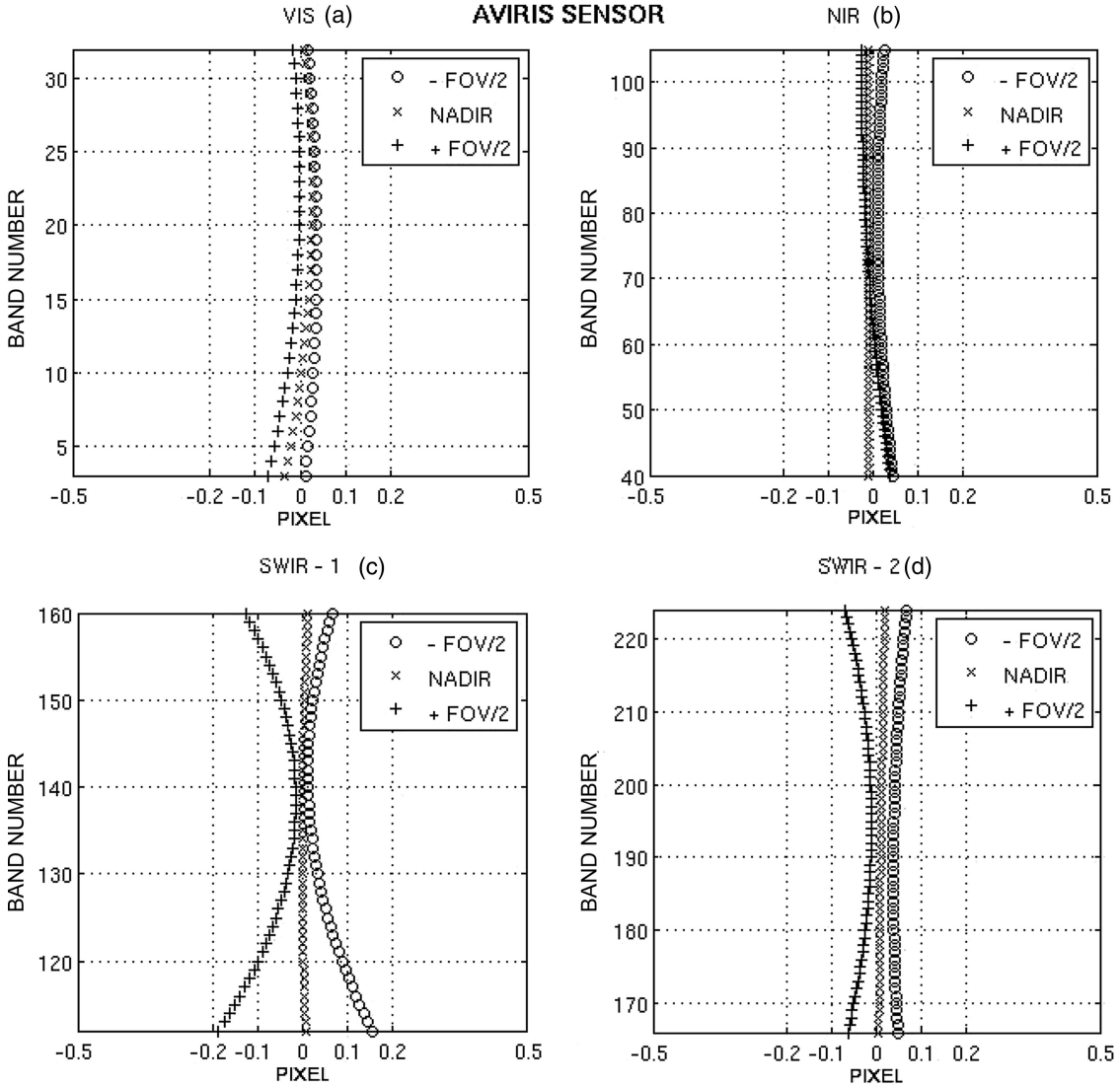

Fig. 12. AVIRIS analysis: Spatial misregistration in this whiskbroom detector is very low, namely under 3% both in the VNIR and in the NIR detectors. The two SWIR detectors present some curvature especially in the positive part of the field of view, and this is probably attributable to some instability. SM is also very low in these two detectors.

utable to the sensor SNR. The fitting lines are symmetrical with respect to both the y axis and the z axis; this means that there are no misalignments within this sensor, i.e., the focal plane center is on the optical axis. These properties let us assume that band number 144 can be used as an offset for the whole SM profile, and, second, that the alignment procedure applied to CASI has been really precise. In any case, this sensor confirms our assumptions concerning the variation relationships.

G. AVIRIS

AVIRIS[27] flew for the first time in 1988. There are four detectors: one in the visible range (VIS), one in the near-infrared (NIR), and two detectors in the shortwave infrared region (SWIR1, and SWIR2). This sensor has a very good SNR profile, and thus all the bands have been considered during this analysis. The scanning method should not provide any kind of SM, and thus it can be used as a benchmark because each ground pixel is recorded separately. The detection procedure produces values that almost superimpose themselves to the fittings lines, and so we decide to show only the fitting curves.

The VIS detector [Fig. 12(a)] exhibits an almost constant SM (i.e., the fitting lines have no curvature) in all the three selected locations along the across-track direction, and it is less, in absolute value, of 2.81% of a pixel size. It is actually what we expected because of the whiskbroom scanning system. The SM is very low, but if we would like to correct for it, we have to take a channel at approximately band number 16, as an offset for the whole array. The NIR detector [Fig. 12(b)] shows the same behavior as the VIS detector. The SM is even less than before: it is lower, in absolute value, than 1.88%. One can also assume that the SM is absent in this sensor. The two SWIR detectors have a spatial misregistration performance, which is a little bit different from the two previous detectors [Figs. 12(c) and 12(d)]. They show, except for the NADIR position, fitting lines that have a certain amount of curvature; this is probably because these two sensors suffer more from airplane instability. Another reason could be the spectral transmittance that is low (approximately 10%) in the last bands of these two detectors, in comparison to the other part of the spectrum. The fittings at $-\mathrm{FOV}/2$, and $+\mathrm{FOV}/2$ have symmetry both around the z axis, and the y axis: this implies that SWIR-1 and SWIR-2 are both aligned and centered with the optical axis; in other words, there are no misalignments. The SM values are higher than before but they are within a very low threshold. The SM for the SWIR-1 detector is, in absolute value, below 6.39% of a pixel size, while for the SWIR-2 detector it is below 4.52%. In general, AVIRIS has the lowest SM if we compare it with the other tested instruments; this confirms our assumptions, and it also gives validity to the proposed scene-based method.

6. Conclusion

Spatial misregistration has been analyzed, and its effect on the quality of data has been shown: If it is higher than 5%–10% of a pixel size then the physical meaning of the recorded spectra can be compromised. Therefore a scene-based detection method has been proposed. SM is mainly detected with laboratory measurements for a few positions along the FOV because it is time consuming. The proposed method allows several locations to be analyzed, provided that edges are apparent within the acquired image cubes. The main advantage of the method is that we do not have to choose any *a priori* reference. The average edge position in a monochromatic view is calculated with respect to an ideal edge. The average position profile has a minimum at a given band, and this can be used as an offset for the position values corresponding to the other bands.

The SM profile is then relative to the lowest SM, which corresponds to one spectral band. If we consider this minimal value as being zero misregistration, a correction scheme can be implemented. The method can be adapted with only a few modifications (e.g., number of across-track pixels and file format) to most of the hyperspectral sensors, such as pushbroom or whiskbroom.

The results show that SM depends both on wavelength, and across-track position: We have been able to identify a quadratic dependence on wavelength for some of the analyzed sensors, while the linear dependence is more or less apparent in each one of them. It is important to notice that SM changes the sign when we cross the z axis.

The fitting lines can be used as a tool to check the alignments within the sensor components; basically they show if vertical and/or rotational misalignments are affecting the focal plane. Laboratory SM measurements were available for two sensors, and when compared them with our results, they suggest that the method can be useful for SM detection.

Most of the analyzed pushbroom sensors use a grating as a dispersing element and often filters to remove high-diffraction orders. When the filter does not cover all the spectral range, a sort of discontinuity appears in the SM profile. This step is located exactly around the band number corresponding to the transition between the filtered and the unfiltered spectral region of the spectrometer.

The tested whiskbroom sensor (AVIRIS) provides a further validation to the procedure. In this case, the SM profile does not follow the same quadratic dependence with wavelength as in the pushbroom scanners. Furthermore, the values are much lower because it records one ground pixel at once, which keeps the interference between the adjacent spectra extremely modest.

A comparison table (Table 2) shows the average SM values for all the tested instruments: The values are expressed as a fraction of the pixel size. It is easy to see that almost all the checked sensors have a very low SM. Generally, it is not higher than 5%,

Table 2. Spatial Misregistration in Different Sensors Expressed as Fraction of a Pixel Size

	−FOV/2	NADIR	+FOV/2
HYSPEX	0.0629	−0.0025	−0.1039
PHILLS	−0.1405	−0.0029	0.2269
AISA	−0.0343	0.0014	0.0841
HYPERION SWIR	0.0511	−0.0028	−0.0232
HYPERION VNIR	0.2261	−0.0046	−0.2296
CHRIS	−0.2002	0.0381	0.2569
CASI3	0.1004	0.0098	−0.1015
AVIRIS VIS	0.0281	0.0112	−0.0184
AVIRIS NIR	0.0188	−0.0099	−0.0054
AVIRIS SWIR1	0.0507	0.0045	−0.0639
AVIRIS SWIR2	0.0452	0.0112	−0.0305

which is supposed to be the operational demanded requirement for SM in hyperspectral sensors. Further developments of the implemented methodology include automatic selection of the subsets needed for SM detection and integration of the procedure in a processing software chain that brings the acquired data from Level-0 to Level-1. This will be fully included in the Airborne Prism Experiment (APEX)[33] data-processing chain.

This work has been supported by the European Space Agency/European Space Research and Technology Centre. The authors thank Ivar Baarstad from the HYSPEX team, Daniel Korwan from the Ocean PHILLS team, and Reno Choi from the UK Environmental Agency for providing data and information about the respective sensors. The authors also thank Pantazis Mouroulis (Jet Propulsion Laboratory), Robert Neville (CCRS), and Andrea Sacchetti (Eidgenössische Technische Hochschule) for the fruitful discussions.

References

1. J. Nieke, H. Schwarzer, A. Neumann, and G. Zimmermann, "Imaging spaceborne and airborne systems in the beginning of the next century," in *Sensors, Systems and Next-Generation Satellites,* H. Fujisada, ed., Proc. SPIE **3221,** 581–592 (1997).
2. J. Fisher, M. Baumback, J. Bowles, J. Grossmann, and J. Antoniades, "Comparison of low-cost hyperspectral sensors," in *Imaging Spectrometry IV,* M. Descour and S. Shen, eds., Proc. SPIE **3438,** 23–30 (1998).
3. R. B. Gomez, "Hyperspectral imaging: a useful technology for transportation analysis," Opt. Eng. **41,** 2137–2143 (2002).
4. S. E. Reichenbach, L. Cao, and R. M. Narayanan, "Information efficiency in hyperspectral imaging system," J. Electron. Imaging **11,** 347–353 (2002).
5. Christophe, D. Léger, and C. Mailhes, "Quality criteria benchmark for hyperspectral imagery," IEEE Trans. Geosci. Remote Sens. **43,** 2103–2113 (2005).
6. P. Mouroulis, R. O. Green, and T. G. Chrien, "Design of pushbroom imaging spectrometers for optimum recovery of spectroscopic and spatial information," Appl. Opt. **39,** 2210–2220 (2000).
7. W. Mao and Y. Xu, "Distortion of optical wedges with a large angle of incidence in a collimated beam," Opt. Eng. **38,** 580–585 (1999).
8. J. M. Sasian, "Aberrations from a prism and a grating," Appl. Opt. **39,** 34–39 (2000).
9. J. M. Sasian, "How to approach the design of a bilateral symmetric optical system," Opt. Eng. **33,** 2045–2061 (1994).
10. W. S. S. Blaschke, "Field aberrations in wide aperture optical systems," Proc. Phys. Soc. London Sect. B **67,** 801–810 (1954).
11. C. Zhao and J. H. Burge, "Conditions for corrections of linear and quadratic field-dependent aberrations in plane-symmetric optical systems," J. Opt. Soc. Am. A **19,** 2467–2472 (2002).
12. W. Mao, "Error and adjustment of reflecting prisms," Opt. Eng. **36,** 3367–3371 (1997).
13. D. Schläpfer, J. Nieke, and K. I. Itten, "Spatial PSF nonuniformity effects in airborne pushbroom imaging spectrometry data," IEEE Trans. Geosci. Remote Sens. (to be published).
14. P. Mouroulis, D. A. Thomas, T. G. Chrien, V. Duval, R. O. Green, J. J. Simmonds, and A. H. Vaughan, "Trade studies in multi/hyperspectral imaging systems final report," Jet Propulsion Laboratory files (29 October 1998).
15. R. O. Green, "Spectral calibration requirement for Earth-looking imaging spectrometers in the solar-reflected spectrum," Appl. Opt. **37,** 683–690 (1998).
16. D. R. Lobb, "Theory of concentric designs for grating spectrometers," Appl. Opt. **33,** 2648–2658 (1994).
17. M. J. Barnsley, J. J. Settle, M. A. Cutter, D. R. Lobb, and F. Teston, "The PROBA/CHRIS mission: A low-cost smallsat for hyperspectral, multi-angle, observations of the Earth surface and atmosphere," IEEE Trans. Geosci. Remote Sen. **42,** 1512–1520 (2004).
18. D. R. Lobb, "Imaging spectrometers using concentric optics," in *Imaging Spectrometry III,* M. R. Descour and S. S. Shen, eds., Proc. SPIE **3118,** 339–347 (1997).
19. J. Nieke, M. Solbring, and A. Neumann, "Noise contributions for imaging spectrometers," Appl. Opt. **38,** 5191–5194 (1999).
20. P. Mouroulis and M. M. McKerns, "Pushbroom imaging spectrometer with high spectroscopic data fidelity: experimental demonstration," Opt. Eng. **39,** 808–816 (2000).
21. M. E. Winter, P. G. Lucey, T. Williams, and M. Wood, "Calibration of the University of Hawaii's airborne hyperspectral imager," in *Imaging Spectrometry IX,* S. S. Shen and P. E. Lewis, eds., Proc. SPIE **5159,** 370–379 (2003).
22. R. A. Neville, L. Sun, and K. Staenz, "Detection of keystone in imaging spectrometer data," in *Algorithms and Technologies for Multispectral, Hyperspectral, and Ultraspectral Imagery X,* S. Shen and P. Lewis, eds., Proc. SPIE **5425,** 208–217 (2004).
23. J. C. Russ, *The Image Processing Handbook,* 4th ed. (CRC Press, 2002).
24. W. Frei and C. Chen, "Fast boundary detection: A generalization and a new algorithm," IEEE Trans. Comput. **10,** 988–998 (1977).
25. J. M. S. Prewitt, "Object enhancement and extraction," in *Picture Processing and Psychopictorics,* B. S. Lipkind and A. Rosenfeld, eds. (Academic, 1970).
26. I. Abdou, *Quantitative Methods of Edge Detection,* USCIPI Report 830, Image Processing Institute (University of Southern California, Los Angeles, 1973).
27. T. G. Chrien, R. O. Green, and M. L. Eastwood, "Accuracy of the spectral and radiometric laboratory calibration of the airborne visible/infrared imaging spectrometer (AVIRIS)," in *Imaging Spectroscopy of the Terrestrial Environment,* G. Vane, ed., Proc. SPIE **1298,** 37–49 (1990).
28. I. Baarstad, T. Løke, and P. Kaspersen, "ASI–A new airborne hyperspectral imager," in *Proceedings of the Fourth EARSel Workshop on Imaging Spectroscopy–New Quality in Environmental Studies* (Warsaw, 2005), pp. 107–110.
29. C. O. Davis, J. Bowles, R. A. Leathers, D. Korwan, T. V. Downes, W. Snyder, W. Rhea, W. Chen, J. Fisher, P. Bissett, and R. A. Reisse, "Ocean PHILLS hyperspectral imager: design, characterization, and calibration," in Opt. Express **10,** 210–221 (2002).

30. R. Bärs, L. Watson, and O. Weatherbee, "AISA as a Tool for Timely Commercial Remote Sensing," in *Fourth International Airborne Remote Sensing Conference and Exhibition* (ERIM, 1999), Vol. I, pp. 239–246.
31. M. A. Folkman, J. Pearlman, B. L. Liao, and P. J. Jarecke, "EO-1/Hyperion hyperspectral imager design, development, characterization, and calibration," in *Hyperspectral Remote Sensing of the Land and Atmosphere,* W. L. Smith and Y. Yasuoka, eds., Proc. SPIE **4151,** 40–51 (2001).
32. S. K. Babey and C. D. Anger, "Compact airborne spectrographic imager (CASI): a progress review," in *Imaging Spectrometry of the Terrestrial Environment,* G. Vane, ed. Proc. SPIE **1937,** 152–163 (1993).
33. J. Nieke, K. I. Itten, W. Debruyn, and the APEX team, "The Airborne Imaging Spectrometer APEX: from concept to realization," in *Proceedings of the Fourth EARSel Workshop on Imaging Spectroscopy—New Quality in Environmental Studies* (Warsaw, 2005), pp. 47–53.